Ceramics International 44 (2018) 3625–3635

Contents lists available at ScienceDirect

Ceramics International

journal homepage: www.elsevier.com/locate/ceramint

Thermal properties and phase stability of Yttria-Stabilized Zirconia (YSZ) coating deposited by Air Plasma Spray onto a Ni-base superalloy

D.F. Zambrano[a,d,*], A. Barrios[a], L.E. Tobón[a], C. Serna[a], P. Gómez[a,b], J.D. Osorio[c], A. Toro[a]

[a] Tribology and Surfaces Group, National University of Colombia, Medellín, Colombia
[b] Empresas Públicas de Medellín, Medellín, Colombia
[c] Facultad de Ingenierías, Ingeniería en Energía, Universidad de Medellín, Medellín, Colombia
[d] Facultad de Ciencias Físicas y Matemáticas - FCFM, Universidad de Chile, Chile

ARTICLE INFO

Keywords:
Thermal analysis
X-Ray Diffraction
Thermal barrier coatings
Microstructural characterization

ABSTRACT

Thermal properties and microstructure characterization of Yttria Stabilized Zirconia (YSZ) Thermal Barrier Coatings (TBCs) deposited by Air Plasma Spray (APS) onto a Ni-base superalloy (Inconel 625) were studied. Two separate sets of tests were performed. The first one consisted in Differential Scanning Calorimetry (DSC) and Thermogravimetric Analysis (TGA) performed over free-standing TC samples detached from TBCs. The second one included the analysis of the cross section of samples heat treated at 1100 °C with holding times of 600, 1000, and 1700 h. The TC porosity was analyzed for different heat treatment conditions so that inter-lamellar, intra-lamellar and globular pores, as well as cracks, were identified and quantified independently. An initial porosity reduction related to inter-lamellar and intra-lamellar pores, as well as cracks, was observed during the first 600 h of heat treatment, due to sintering. However, porosity continually increased during heat treatment from 600 to 1700 h driven by volumetric changes associated to phase transformations. During this period, yttrium diffused from the metastable tetragonal phase favoring the transformation to cubic phase while monoclinic phase transformed after cooling from the yttrium-depleted tetragonal phase. Energy absorption curves and the variation of heat capacity with temperature were also determined and correlated to microstructural changes.

1. Introduction

Thermal Barrier Coatings (TBCs) define the operational limits and capabilities of gas turbines. The overall performance of such machines is determined by the morphology and microstructural behavior of the Top Coat (TC) when it operates at high temperature. One of the most widely used materials for the TC, particularly in land-based gas turbines, has been 7–8 wt% Yttria-Stabilized Zirconia (YSZ) applied by Atmospheric Plasma Spray (APS) [1]. During turbine operation, the TBCs undergo microstructural and morphological changes. Long-term operation eventually causes a detriment of the TC integrity affecting the mechanical and thermal properties, which directly impacts the reliability of components located in hot gas paths [2]. The lack of precise knowledge about the evolution of the TC microstructure under specific operation regimes (specially non-steady turbine operation) leads to an increment in the repairing costs, as well as a reduction in the efficiency in power generation [2,3]. Determining microstructural and morphological variations of the TC and their effect on the thermal properties under conditions similar to those of operation at gas turbines provides valuable information about thermal efficiency and expected lifetime [4,5]. The variation in thermal properties of YSZ, such as the specific heat at constant pressure (C_p) and the enthalpy of physical-chemical reactions, determine the level of TC degradation and its thermal protection capabilities [6,7]. Wang et al., for instance, reported C_p values between 0.51 ± 0.01 and $0.69 \pm 0.02\ J\,g^{-1}\,K^{-1}$ and thermal conductivity ranging from 1.9 to $2.4\ W\,m^{-1}\,K^{-1}$ for YSZ coatings studied from room temperature up to 1200 °C [5,8].

The relationship between phase transformations and thermal properties plays a significant role on the turbine efficiency and helps to determine when the components must be repaired or replaced. Furthermore, the evolution of the TC morphology has a strong influence on both the thermal conductivity variation and thermo-mechanical properties [9,10]. In consequence, microstructure and morphology of the YSZ-TC must be considered in order to understand their effect on the heat transfer in TBC systems [1,11].

Several works have studied the reduction in thermal conductivity of TBCs due to phonon scattering caused by the increase in the absolute porosity, which reveals the importance of correlating the TC morphology with its thermal properties [6,12,13]. Also, the amount of pores, their morphology, as well as the cracks within the TC generate

* Corresponding author.
E-mail address: dfzambranom@unal.edu.co (D.F. Zambrano).

https://doi.org/10.1016/j.ceramint.2017.11.109
Received 22 August 2017; Received in revised form 27 October 2017; Accepted 15 November 2017
Available online 20 November 2017

variations in C_P, absorbed energy and thermal conductivity, which are influenced by operating temperatures and pressures [14]. The contribution of conduction and radiation to the heat transfer throughout the porous TC must also be considered to track the evolution of thermal properties under operating conditions. For instance, fine-sized pores cause a decrease in the thermal conductivity close to room temperature. At high temperatures and low pressures, instead, they increase "the air thermal conductivity". Since the conduction mechanisms are influenced by large size globular pores and cracks [14,15], the increase in the number of small pores intensifies the phonon scattering that reduces the TC thermal conductivity [12,15,16]. It is also worth mentioning that some fine-sized pores tend to close under operating conditions due to sintering effects [17].

Variations in the microstructure of YSZ-TC can be monitored with the aid of X-Ray Diffraction (XRD) [18] and neutron diffraction [19]. These techniques can be used to determine the influence of the presence of cubic phase (**c**-YSZ), the yttria content, and the degree of stabilization of tetragonal phases (t-YSZ and t′-YSZ) on heat absorption, among other effects. It has been demonstrated, for instance, that the yttria content depletion from the tetragonal phase during operation favors the transformation of this phase into cubic and monoclinic phases [20]. Several authors have carried out high-temperature XRD studies on TCs deposited by Electron Beam-Physical Vapor Deposition (EB-PVD) and Atmospheric Plasma Spray (APS). It is well known the fact that when the non-transformable tetragonal phase (*t′*) is deficient in yttria it may decompose to tetragonal phase with low yttria content (*t*), which is more susceptible to transform to cubic phase with higher yttria content [21,22]. Transmission Electron Microscopy (TEM) has allowed identifying phase transformations in EB-PVD TC samples after being exposed to temperatures from 1100 to 1500 °C [23]. In this case, metastable tetragonal YSZ phases with low and high yttria contents are formed, and the cubic phase is enriched with yttria. Computer-aided simulation using data obtained from TEM has shown that grain boundaries of the cubic structure have a relatively high concentration of yttrium ions [24].

High-temperature characterization of thermal properties and microstructure of APS-deposited 7–8% YSZ-TC samples is conducted in this work with special interest in the influence of cooling and heating rates (which somewhat resemble non-steady turbine operation) on the aforesaid properties. Characterization techniques including high-temperature XRD (up to 1050 °C), Differential Scanning Calorimetry (DSC) and Thermogravimetric Analysis (TGA) (up to 1300 °C) allowed assessing the changes in phase contents, specific heat, thermal conductivity and enthalpy of the TC.

2. Materials and methods

The TBC system studied in this work consisted of Inconel 625 substrate, MCrAlY bond coat applied by High Velocity Oxygen Fuel (HVOF) and 7 wt% Y_2O_3-ZrO_2 top coat deposited by APS. The manufacturing process for the TC used feedstock of vacuum-atomized spherical particles with an average diameter of ~ 60 μm (minimum size 45 μm, maximum size 90 μm), containing circa 68.8 wt% Zr, 31.4 wt% O and 5.8 wt% Y; for the bond coat (BC), the powders consisted of vacuum-atomized spherical particles with an average diameter of 45 μm (minimum size 10 μm, maximum size 60 μm), which were mainly composed of Ni (48.4 wt%), Co (23.1 wt%), Cr (21.9 wt%), Al (5.5 wt %) and O (1.2 wt%). Prior to deposition, the metallic substrate was sand blasted in order to obtain a surface texture with arithmetic mean roughness (Ra) between 3 and 6 μm. HVOF bond coat deposition was done with oxygen flow rate of 4 $m^3\,s^{-1}$, propylene flow rate of 1 $m^3\,s^{-1}$ and the standoff distance was 0.4 m for the spraying. In turn, the top coat was applied using a D.C. plasma torch with anode-nozzle internal diameter of 8 mm, plasma current of 600 A, plasma voltage of 70 V, injection angle of 90°, stand-off distance of 0.9 m and a flow rate of 8.3 $m^3\,s^{-1}$ Ar and 2.5 $m^3\,s^{-1}$ H_2.

2.1. Samples preparation

Two sets of samples were prepared as described below:

i) Free-standing TC samples were detached from the TBC system in order to perform analyses by DSC, TGA, High Temperature X-Ray Diffraction (XRD) and Optical (OM) and Scanning Electron Microscopy (SEM) equipped with Energy-Dispersive X-ray Spectroscopy (EDXS) and Wavelength-Dispersive X-ray Spectroscopy (WDXS) detectors.
ii) Cross sections of TBC samples were vacuum-impregnated in a phenolic resin, ground with emery papers and polished in clothes with diamond particles in order to perform microstructure assessment using XRD together with OM and SEM.

The detachment of the TC specimens from the rest of the TBC system was carried out by controlled chemical dissolution in an acidic aqueous solution (pH 1.5) consisting of 13.2 g $FeCl_3$ + 75 g HCl + 3 g HNO_3 + 22 g deionized water. A surfactant was added in order to reduce the exposure time to the acidic aqueous solution. The sample was exposed to the solution during 5.5 h at 65 °C. In order to remove contaminants, the free-standing TC specimen was cleaned after the detachment process using a basic aqueous solution (pH 7.5) consisting of amines with inorganic fluoride salts at 80 °C during 15 min.

2.2. Thermal analysis and microstructure characterization

The specific heat capacity and enthalpy of the free-standing TC samples were measured at constant pressure using a simultaneous TGA/DSC (SDT) analyzer (TA Instruments, model Q600) with the aid of Universal Analysis® software (TA Instruments). Free-standing TC specimens of 4 × 4 mm and 30 ± 0.1 mg were placed in Al_2O_3 crucibles for TGA/DSC measurements. The specific heat was determined by heating the samples from room temperature to 1450 °C using a sapphire standard reference material. The heating rates were 10, 15 and 20 °C min^{-1}. The C_P was calculated according to the ASTM E-1269 standard [25].

A JEOL 5910LV SEM was used to obtain TBC cross-sectional images. Chemical microanalysis were performed using EDXS and WDXS spectrometers. XRD patterns were obtained in free-standing samples using a Panalytical X'Pert PRO X-ray diffractometer with monochromatic CuKα (λ = 1.5406 Å) radiation. The diffraction patterns were obtained within the $15° \leq 2\theta \leq 90°$ range and step of 0.013° s^{-1} using a standard θ–2θ Bragg-Brentano geometry. Rietveld refinement was performed to measure the phases at different conditions. This analysis was complemented with the General Structure Analysis System (GSAS) package and the EXPGUI interface and included a chi-squared fit of 3.1 ± 0.5 [26,27]. The XRD patterns for the TC were obtained at 100, 200, 400, 600, 800, and 1050 °C both during heating and cooling cycles, with holding time of 10 min at each temperature. The heating rate was set to 10 °C min^{-1} while the cooling rate was determined by the thermal insulation of the equipment as shown in Fig. 1. The temperatures were selected to emulate temperature variations experienced by a gas turbine under operating conditions. In order to analyze phase changes in the TC during longer exposure times at high temperatures, additional X-Ray and porosity analyses were performed for samples exposed at 1100 °C during 600, 1000, and 1700 h. Analyses over an as-sprayed sample at room temperature were also considered for reference purposes.

Four YSZ phases were used for interpretation of the XRD patterns: stable (t′) and metastable (t) tetragonal phases, cubic phase (c) and monoclinic phase (m). The yttria content of the tetragonal phase was calculated using Eq. (1) [20], where *a* and *c* are the tetragonal lattice parameters in angstroms. This information was combined with the results from XRD analyses in order to study the stability of the phase with temperature.

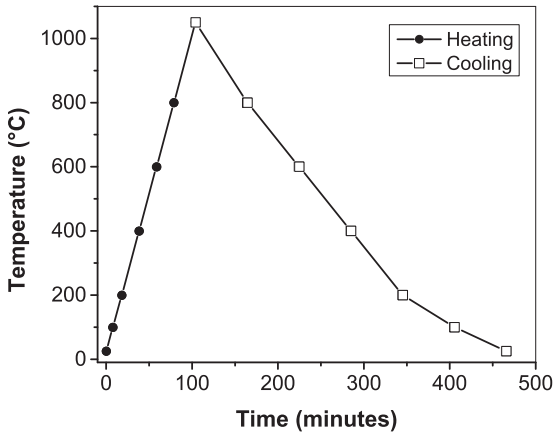

Fig. 1. Heating and cooling curves of TC samples during XRD tests. The X-Ray diffractograms were obtained at the temperatures represented by dots (during heating cycle) or squares (during cooling cycle) in the graph.

$$YO_{1.5}\ (\text{mol\%}) = \frac{1.0225 - \frac{c}{a\sqrt{2}}}{0.001311} \quad (1)$$

2.3. Porosity and morphology

Morphological attributes of the TC such as pores, cracks, inter-lamellar, intra-lamellar, and trans-lamellar contacts (also known as pore-voids) are usually classified according to their size, location, geometry, and aspect ratio [28,29]. Columnar grains are found inside splats with an specific pore distribution. This distribution is mainly globular with small pores (< 10 μm). Angular and/or medium size pores could also be found in a less extent [29,30]. In this study, the porosity analysis was carried out for as-sprayed and thermally treated samples at 1100 °C for 600, 1000, and 1700 h. The pore classification criterium used in this work is presented in Table 1. The obtained results were correlated with those found from the phase transformation analysis.

The porosity was analyzed in detail and individual pores were classified depending on their shape and distribution in the microstructure (see Table 1). Cross-sectional images were taken with the aid of a Nikon Eclipse LV100 optical microscope equipped with a CCD camera with a resolution of 1600 × 1200 pixels, which represents a work area of 193 × 145 μm^2 in each micrograph. All the images were converted to 8 bits and then normalized, and the magnification was chosen in such a way that the whole TBC was observed in each cross-sectional field following recommendations found in ASTM E2109-01 standard.

In order to correct the non-homogeneous distribution of light over the sample, which is typical of optical microscopes, the Sauvola algorithm [31] was used during the segmentation process with a working window of 80 pixels and K = 0.1. Afterwards, binary operations and shape factors were applied to identify the defects in the microstructure including globular, inter-splat and intra-splats pores, as well as cracks. The segmented images containing information of all the porosity "objects" were modified by applying the Boolean function OPEN to remove the inter- and intra-splat pores. The segmented images were then subtracted from the modified ones so the resulting images contained information regarding the globular pores. Finally, to differentiate cracks from pores, an "aspect ratio - size" filter was applied; then, the remaining cracks (that were not possible to separate automatically because they were linked to the pores in the segmented images) were manually cut. Fig. 2 shows the typical results of the digital processing steps implemented to characterize the porosity of the samples.

3. Results and discussion

3.1. Microstructure evolution of the TBC system after high-temperature exposition

The studied TBC system has a typical structure composed of TC, BC and substrate, which can be clearly identified by SEM examination as shown in Fig. 3. The TC showed an Yttrium content of 7.25 ± 1.35 wt% measured by EDXS and WDXS. The BC is of the NiCrCoAlY type. The chemical analysis of the Ni-based superalloy yielded 54.92 ± 2.43 wt% Ni, 21.13 ± 1.12 wt% Cr, 20.94 ± 2.05 wt% Co, 2.22 ± 1.02 wt% Ti, and 0.79 ± 0.82 wt% Mo. TC's and BC's thicknesses were 260.6 ± 25.4 and 80 ± 30 μm respectively. A thin α-Al_2O_3 layer (TGO layer) is also observed between the BC and the TC, whose growth was favored by the oxygen reaction with aluminum from the BC at high activation energies during the APS deposition process [32,33].

Globular, inter-lamellar, and intra-lamellar pores, as well as cracks, were found in the TC in as-sprayed and heat treated conditions. The surface morphology of the TC showed well-defined splats with pre-cracking, Fig. 4a. In Fig. 4b, the cross-sectional image clearly shows inter-lamellae contact and fine columnar grains which were formed during lamellae quenching after the plasma spraying process.

The typical aspect of the microstructure of both as-sprayed and heat treated TBC samples is presented in Fig. 5. Results for the porosity analysis over these samples are presented in Figs. 6 and 7. The porosity was sorted according the classification presented in Table 1.

3.1.1. Inter-lamellar, intra-lamellar pores and cracks

In the as-sprayed condition, on average more than 600 objects (inter-/intra- pores and cracks) were found on each measurement field with size 193 μm by 145 μm. During the first 600 h of heat treatment at 1100 °C sinterization takes place, rapidly reducing the amount of small elongated pores such as inter- and intra-lamellar reaching about 150 objects, as can be observed in Fig. 6a, b, and 7a. This sintering effect has been widely reported in the literature [29,34]. After 600 h, inter-lamellar and intra-lamellar pores and cracks start to increase reaching about 360 objects and passing from around 750–1300 μm accumulated length after 1700 h, as can be seen in Fig. 7a and b. After the sinterization process the TC becomes denser, reducing its capacity to absorb energy due to thermal expansion and deformation. At this time, the diffusion processes favored by the exposure time at a high temperature promote the transformation of a fraction of the tetragonal phase into monoclinic after cooling. This phase transformation is analyzed later in this paper. The tetragonal to monoclinic transformation has associated volumetric changes in the denser TC causing an increment in inter-

Table 1
Porosity classification used in this work.

Type of porosity	Projected pore size in cross-sectional view	Main features
Globular pores	1–10 μm^2	Mainly located into splats
	10–100 μm^2	Located into and between splats/lamellae
	> 100 μm^2	Mainly located between splats/lamellae
Elongated pores: Inter-, intra-, and trans-lamellar pores	Various sizes	Separated from globular pores by aspect ratio, minimum and maximum radius.
Elongated pores: Cracks	Various sizes	Located across the whole TC

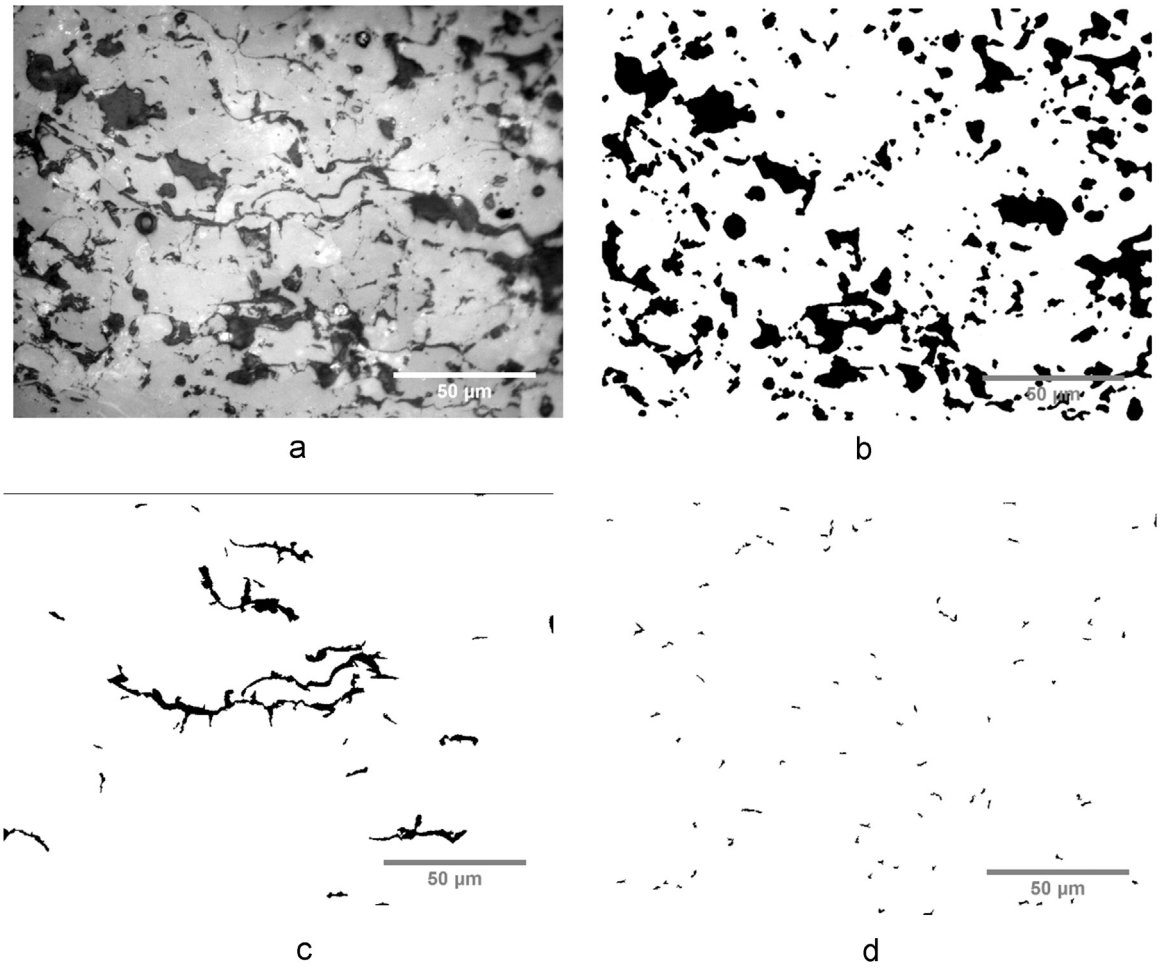

Fig. 2. a) Cross-sectional view of as-sprayed TC (gray scale), b) segmented globular pores c) segmented cracks d) segmented inter-lamellar and intra-lamellar pores.

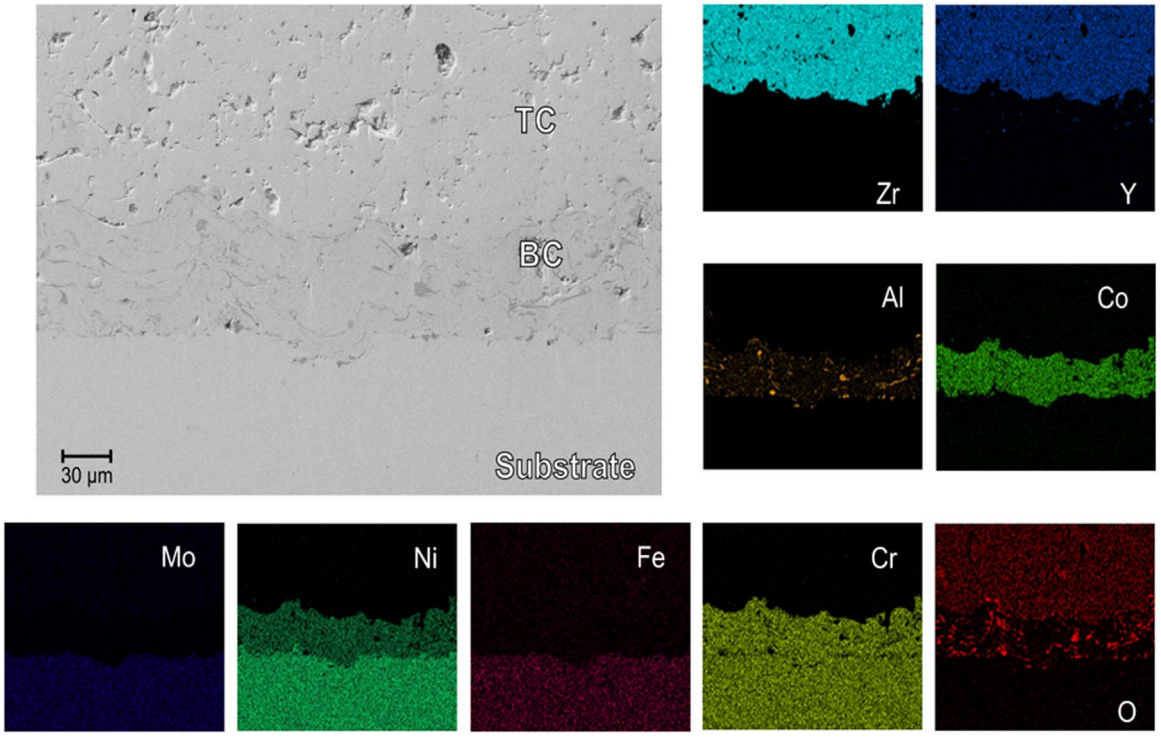

Fig. 3. SEM micrograph (up left) and EDXS compositional maps of as-sprayed TBC system.

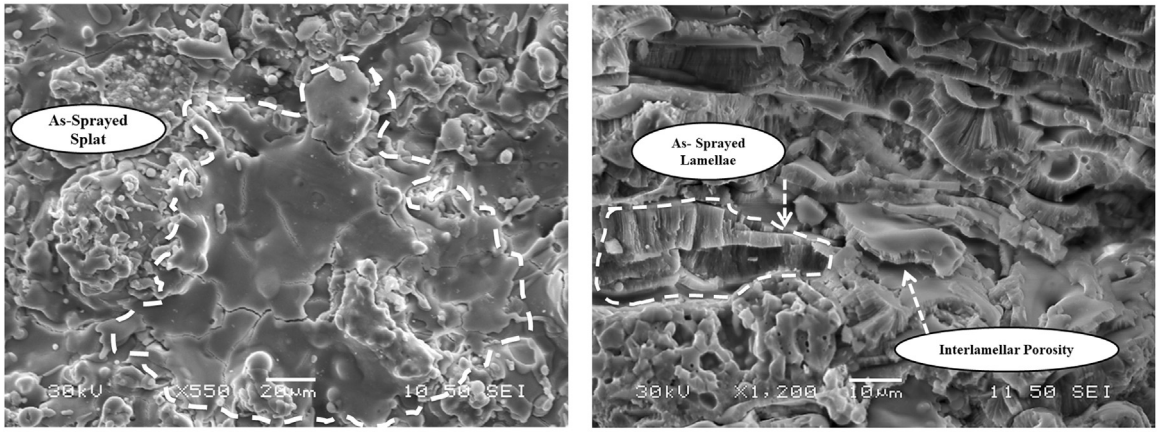

Fig. 4. As-sprayed TC morphology; a) Splat on TC surface with pre-cracking; b) TC's cross-section showing lamellae and their columnar grains.

lamellar, intra-lamellar pores and cracks, i.e. the increase in cracking is a consequence of a lower capacity of the TC to adjust the volumetric changes associated with the phase transformation. Microstructure changes (Figs. 6 and 7) with the heat treatment have also been reported elsewhere [34–36].

3.1.2. Globular pores

Fig. 7 shows the variation of the number of pores and the porosity percentage with exposition time to 1100 °C. In general, it was observed a porosity reduction in the first 1000 h caused by diffusion in the TC. Afterwards, phase transformations appeared in opposition to sintering process. However, a more detailed analysis of the evolution of the number of pores indicates that the number of large pores ($> 100\ \mu m^2$) remained approximately stable with time, while in the case of medium size ($10–100\ \mu m^2$) and small pores ($10–100\ \mu m^2$) there was a slight reduction up to 600–1000 h followed by an increase until 1700 h. This

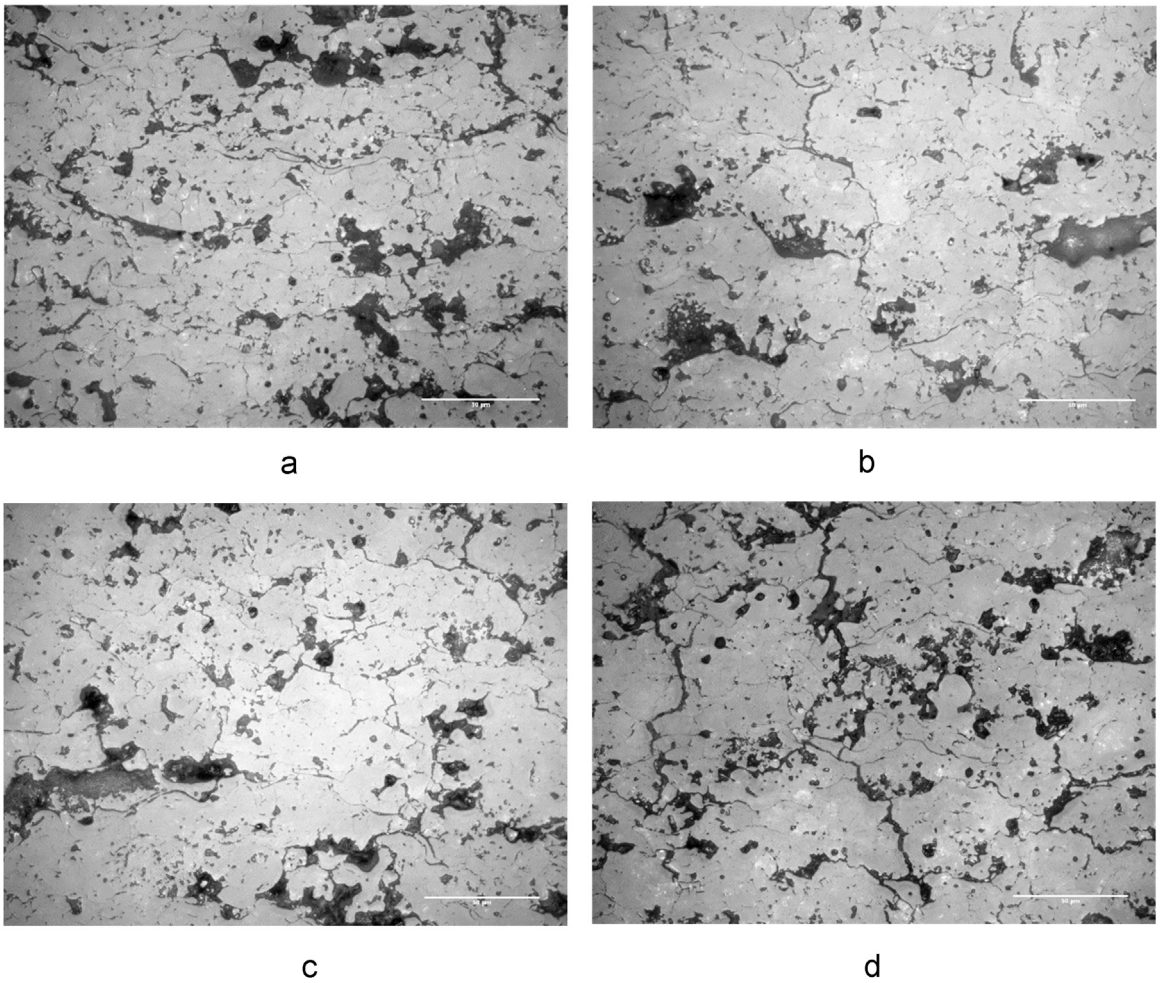

Fig. 5. TBC micrographs for as-sprayed (a) and heat treated samples at 1100 °C with exposure time of: b) 600 h, c) 1000 h, d) 1700 h.

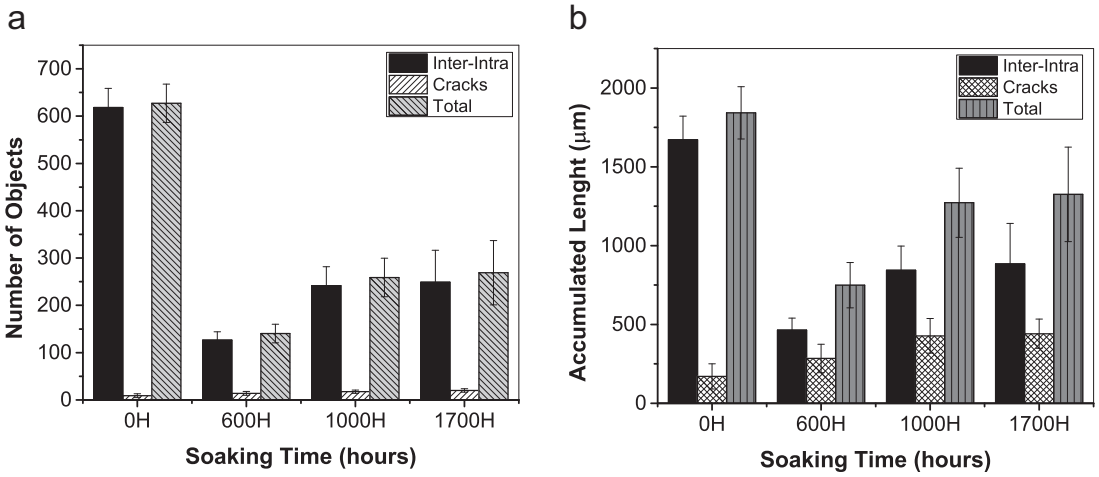

Fig. 6. a) Number of pores and b) accumulated length of inter-lamellar, intra-lamellar pores and cracks.

is consistent with the shape changes and pore size reduction through necking and cohesion that have been reported in previous works [36–38].

Regarding the porosity percentage, large pores (> 100 μm^2) showed an initial increase in size because of coalescence with cracks, however, there was a general reduction until 1700 h. Porosity related to medium (10–100 μm^2) and small (1–10 μm^2) pores showed a reduction reaching 1000 h and then, a slight increment to 1700 h. The area-to-volume ratio of these pores confers them more specific area and therefore more energy available to be closed during splat/lamellae stiffening. Figs. 2 and 4 show that the majority of small pores are isolated from other pores or cracks, so they tend to close due to diffusion of vacancies, mass transfer through grain boundaries (into the splat), inter-/intra- splat contact corners and controlled grain growth. However, if the grain growth rate is too high, the grain boundaries can move faster than pores and then isolate them within the grains. Furthermore, if the grain continues to grow, globular pores cannot be eliminated, which explains the increase in globular porosity at 1700 h. This behavior is consistent with the fact that the cation diffusion coefficient in zirconia is orders of magnitude smaller than that of the oxygen anions, which leads to accumulation of Y^{3+} cations and reduction of mobility of oxygen anions at the grain boundaries. As a consequence, oxygen anion transport is also restricted to the inter-splat contact and microcracks despite their larger amount of surface available, then the required time to reduce the volume fraction of inter-lamellar pores increases.

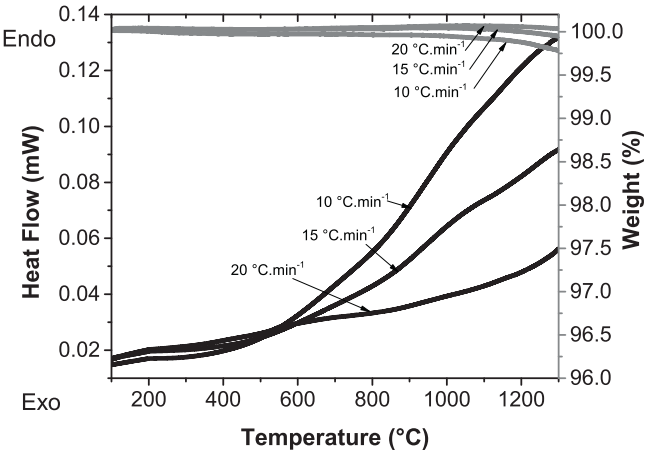

Fig. 8. Effect of heating rate on DSC-TGA curves for as-sprayed TC.

3.2. Variation of thermal properties

The effect of the heating rate on the energy absorption and mass loss of the as-sprayed TC sample is shown in Fig. 8. The samples tested with heating rates of 10 and 20 °C min^{-1} had a very similar behavior. A change in the slope of heat flow curves is observed in the temperature range of 450 °C and 500 °C for heating rates of 10 °C min^{-1} and

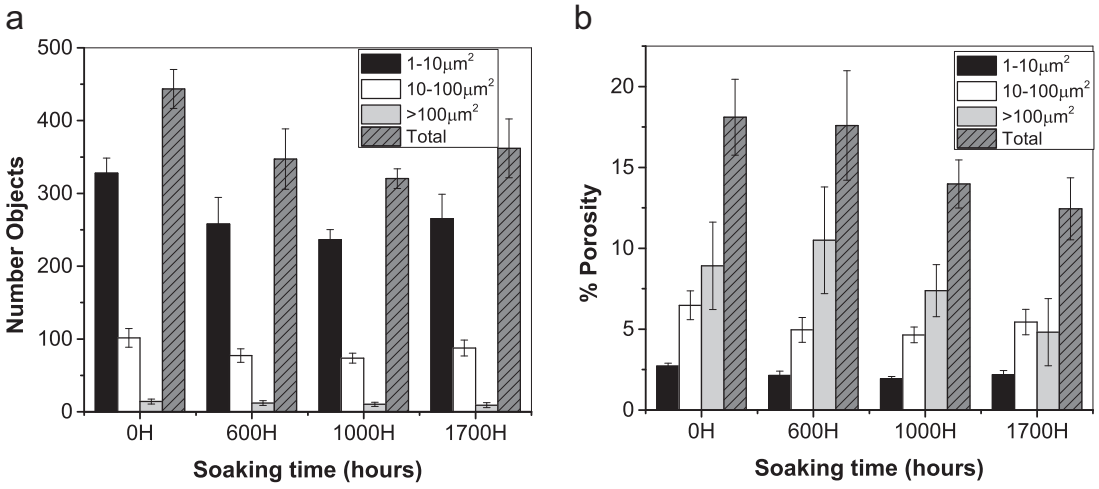

Fig. 7. a) Number of globular pores and b) total percentage of globular pores as a function of soaking time at 1100 °C.

15 °C min^{-1}. For a heating rate of 20 °C min^{-1} there is no clear evidence of a change in the slope. Some studies reported in the literature have found that the TC composition lies within the cubic phase stability region at the synthesis temperature [39]. Tetragonal phase is usually obtained as a second phase during crystallization when the yttrium distribution in the cubic phase is not homogeneous and the synthesis procedure was designed to avoid the formation of tetragonal traces [39]. Comparing with XRD results from this work, the large amount was the tetragonal phase. In addition, there was no evidence of endothermic or exothermic peaks despite the heat flow increases at temperatures above 500 °C generating changes in the slope. This behavior is probably caused by phase transitions of tetragonal and cubic phases. On the other hand, the weight loss obtained by TGA is not significant, which indicates that contamination of the sample after the chemical treatments is minimal.

The total enthalpy change between room temperature and 1300 °C was 2.85 J g^{-1}; this means that the absorbed heat and the thermal conductivity in the YSZ structure increased [5,10]. This behavior was related to the increase in the specific heat capacity at high temperatures due to the difference in lattice parameters between the mixed oxides (ZrO_2 and Y_2O_3), which is responsible for volumetric changes and therefore variations in the vibrational frequencies of the oxides represented by the Neumann-Kopp rule [6], see Table 2.

Fig. 9 shows the variation of the specific heat C_p as a function of temperature for the free-standing TC. The C_p of the sample increases with temperature describing a typical curve [5,40–42]. However, the effect is more relevant at high temperatures, where the variations in C_p and thermal conductivity are expected to affect drastically the power generation efficiency [16].

As seen in Fig. 9, the C_p of as-sprayed TC for the temperature range between 25 and 1197 °C rises from 0.10 ± 0.04 to 0.40 ± 0.08 J g^{-1} K^{-1} [7,43]. However, no significant effect of the different heating rate conditions on the C_p value was observed since its behavior is mainly controlled by the chemistry and crystal structure of YSZ. Generally speaking, the variations in C_p values are related to morphological changes, microstructure and yttrium distribution in the TC. According to Tojo et al. [44], such variations may be the result of a lattice vibration softening, which proceeds following two different mechanisms: the first one is the substitution of yttrium ions or oxygen vacancies leading to different modes of lattice vibrations with respect to natural vibrations in pure zirconia. The second one is the difference in the arrangements of the atoms in the cubic and tetragonal structures, which leads to different interactions and lattice vibrations [44]. The larger values of Cp measured at higher temperatures are consistent with the increase of the amount of cubic phase in the microstructure, as reported previously by McPherson [45] and Tzimas et al. [46].

3.3. Analysis of phase stability in the TC

Fig. 10 shows an XRD pattern for the TC at room temperature in which the peak intensities correspond to metastable (t) and stable (t′) tetragonal phases, as well as cubic phase (*c*). After Rietveld refinement it was found that 95 wt%, 3 wt% and 2 wt% correspond to *t´*, *t* and cubic phases, respectively. These values are similar to those reported in literature [20]. No monoclinic phase was found in the as-sprayed

Table 2
DSC and TGA data for the as-sprayed TC at different rate heat conditions: 10, 15 and 20 °C min^{-1}, between room temperature and 1300 °C.

Rate heating, °C min^{-1}	Enthalpy, J g^{-1}	Mass loss, wt%[a]
10	3.659 ± 0.03	0.055 ± 0.11
15	2.479 ± 0.09	0.073 ± 0.18
20	1.018 ± 0.07	0.065 ± 0.15

[a] Refers to the relative variation of the mass of the samples at the end of the test.

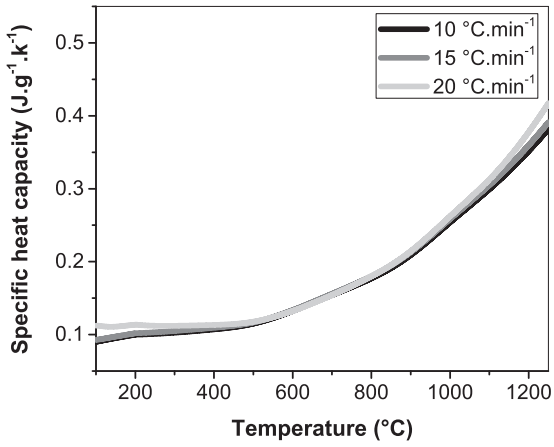

Fig. 9. Specific heat capacity measurements of as-sprayed TC samples for heating rates of 10 °C min^{-1}, 15 °C min^{-1} and 20 °C min^{-1}.

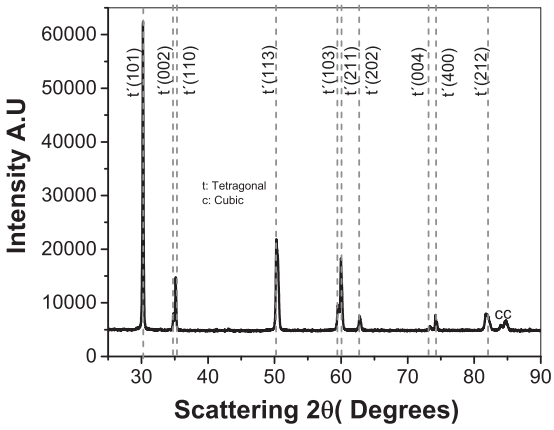

Fig. 10. X-Ray Diffractogram for the as-sprayed TC at room temperature.

Table 3
Phases contents in the TC and amount of $YO_{1.5}$ in the tetragonal phase for different heat treatment conditions. Data obtained by Rietveld refinement applied to XRD patterns taken after different exposure times to 1100 °C.

Time (h)	*t* (wt%)	*c* (wt%)	*m* (wt%)	$YO_{1.5}$ in *t* phase (mol%)
0	99.9	0.1	0.0	7.79
600	86.4	13.6	0.4	6.73
1000	66.3	15.7	18.0	6.43
1700	61.1	15.5	23.4	6.28

condition. This result is expected because the $YO_{1.5}$ content in the tetragonal phase for this condition yields ~ 7.79 mol% (as it is shown later in Table 3) which lies within the stabilization range where no tetragonal to monoclinic transformation occurs during cooling to room temperature.

X-Ray diffractograms of the TC obtained at high temperatures are presented in Fig. 11. The heating and cooling procedure as well as the temperatures where the X-Ray analyses were conducted are illustrated in Fig. 2. Fig. 11a compares changes in the Bragg´s diffraction angle with temperature for a group of peaks between 71.5° and 75.5°, while variations of intensities of the peaks are displayed in Fig. 11b. From Fig. 11a, the peaks exhibit a shift towards lower diffraction angles (left) as the temperature increases. In particular, the main peak t′(400) shifts from 74.2° to 73.4° when the temperature raises from room temperature to 1050 °C. Then, during cooling the peaks move back to a position close (but not identical) to the initial diffraction angle. The peaks' shift with the temperature is related to the thermal expansion of the material which implies an increment of the interplanar distance and

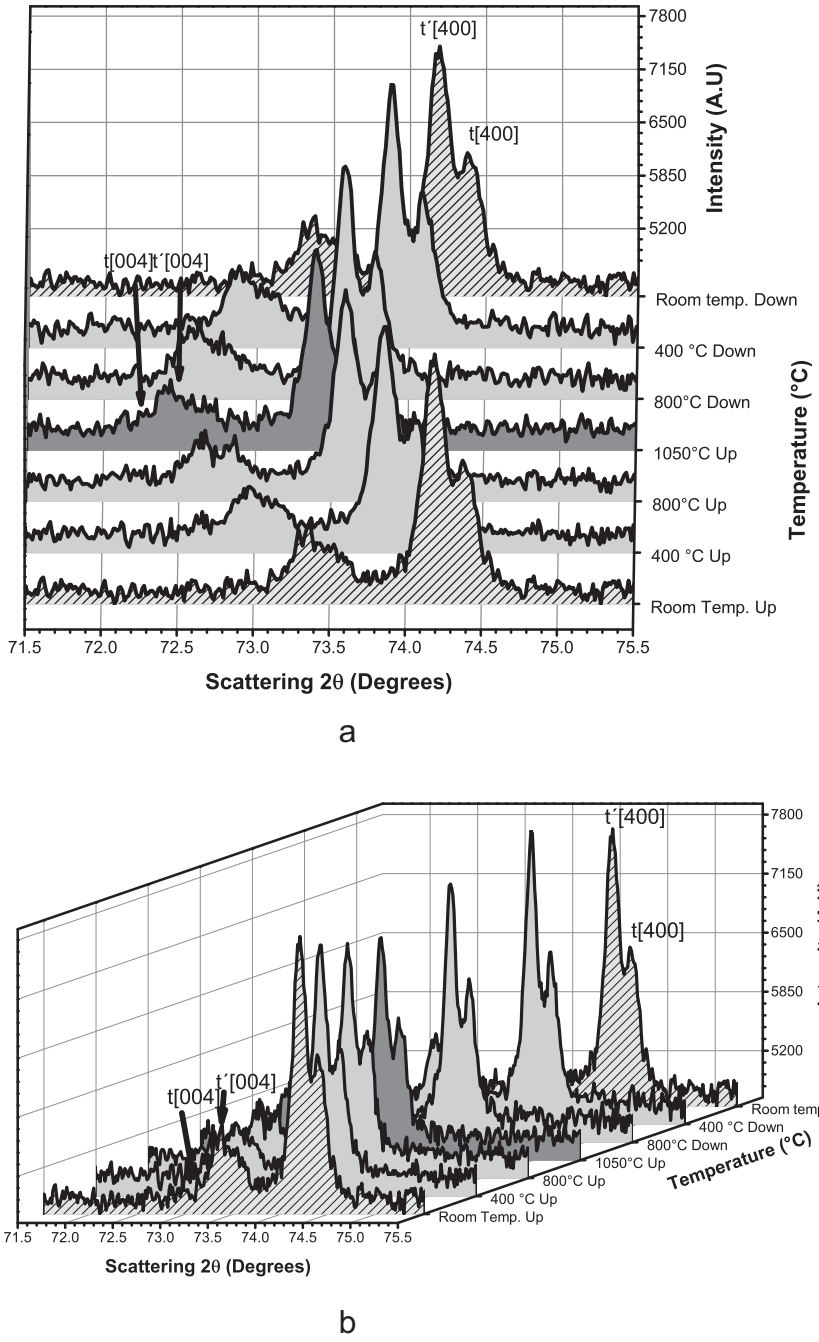

Fig. 11. In situ X-Ray Diffraction patterns for the TC in the range of 2θ from 72.5° to 75.5° during heating and cooling cycles between room temperature and 1050 °C; a) Peak shift effects, and b) changes in intensity.

consequently lower Bragg diffraction angles. On the other hand, the slight change in the position of the peaks at the same temperature for heating and cooling curves is a consequence of diffusion of yttrium leading to a phase destabilization, which is not fully reversible. These microstructural changes generated during the heating and cooling processes are illustrated through the variation in the c/a relation of the tetragonal phase, see Fig. 12, and the change in the Y_2O_3 content in the tetragonal phase, see Fig. 13. Similar results were reported by Wu et al. [5]. The effect of this transformation during the heating and cooling cycles can be observed in the change of intensity of the peaks as can be seen in Fig. 11b. During heating, a small fraction of yttrium diffuses from the tetragonal phase to stabilize the cubic phase. During cooling, on the other hand, not all the already transformed cubic phase is stable at lower temperatures and a re-stabilization of the tetragonal phase occurs.

Fig. 13 shows that, during heating, the yttria content of the tetragonal phase reduces as consequence of diffusion of Y^{3+} and O^{2-} ions and subsequent stabilization of the cubic phase. During cooling the reverse process occur but the composition of the tetragonal phase is not fully restored, mainly because of the increase in activation energy for diffusion due to the creation of new microstructural defects. The actual increment of the amount of cubic phase after thermal cycling leads to a change in the volume of the TC of about 6%. Such volumetric changes are commonly reported in the literature as a cause of delamination and spallation [47,48].

Rietveld measurements of the phase content in the TC during heating and cooling are presented in Fig. 14. Changes in the phase distribution during heating can be appreciated. In particular, at 800 °C the TC was composed by 88.8% *t´*-YSZ and 10.2% *c*-YSZ. At 1050 °C, the amount of cubic phase slightly increased to 10.9% with preferential (111) orientation. The *t´* phase remains almost unvariable (see Fig. 14a) and the small increment in the cubic phase from 800 °C to 1050 °C is

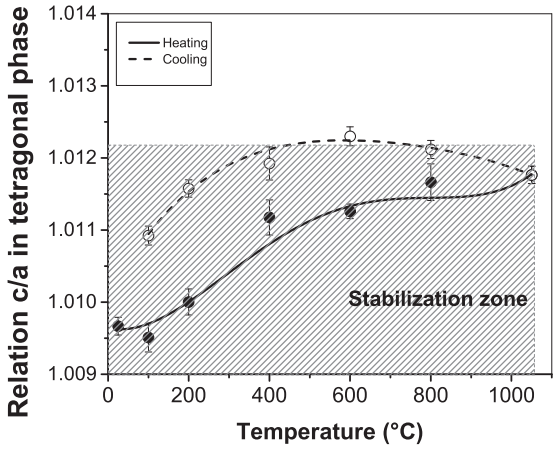

Fig. 12. Variation of c/a ratio of tetragonal phase during heating and cooling in the TC.

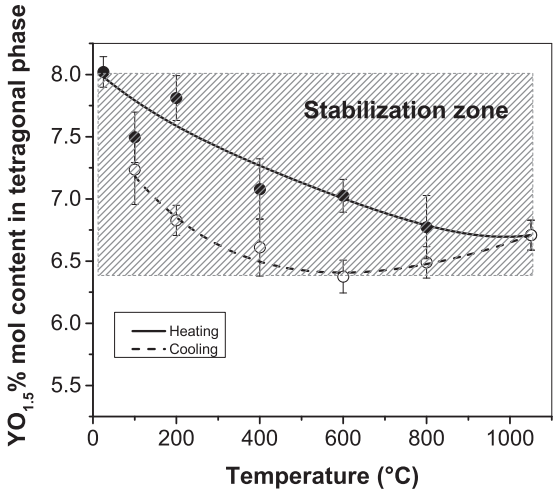

Fig. 13. Variation of yttria content in the tetragonal phase of as-sprayed TC as a function of temperature. Measurements performed by WDXS coupled to SEM.

caused by destabilization of the *t* phase. This result is in agreement with the phase stability analysis since the c/a ratio during heating lies within the *t´*-YSZ stabilization zone, as can be observed in Fig. 12. The c/a values raised from 1.0096 to 1.0117 which means that there is an increase in the tetragonality during heating. Changes in the c/a ratio are more drastic during cooling (the heating rate was 10 °C min^{-1} while the cooling rate was that established by the insulation of the XRD chamber) and a maximum value of 1.0123 around 600 °C was obtained, which is slightly out of the stabilization zone, and then it dropped to 1.0109 at 100 °C. The fact that different concentrations of yttria in the tetragonal phases (8–7 mol% $YO_{1.5}$ for *t´* and 5–4 mol% $YO_{1.5}$ for *t*) leads to a measurable variation in lattice parameters agrees with the results reported in the literature [20] and constitutes the key reason to rely on careful Rietveld analysis to distinguish between stable, high yttria content t´ phase and metastable, low yttria content t phase. Furthermore, the results show that, with the appropriate XRD data processing, unambiguous identification of stable and metastable phases can be performed with the aid of Rietveld refinement even for weight fractions as low as 2–3%.

Fig. 14 also shows the high degree of stabilization of the *t´*-YSZ phase in the as-sprayed TC. Only about 10 wt% of this phase is transformed to *c*-YSZ with the increase in temperature (see Fig. 14a), and practically all of it returned to *t´*-YSZ during cooling (see Fig. 14b) The low yttria content in the metastable tetragonal phase (t-YSZ) induces dimensional changes in lattice parameters of the stable tetragonal phase (t´-YSZ) which begins to destabilize and transforms into the cubic phase. Generally speaking, the major microstructural instabilities caused by tetragonal-to-cubic YSZ phase transformations occur when temperature increased from 400 to 800 °C. The phase transformations that take place in the TC during heating and cooling cycles induce abrupt volumetric fluctuations that can lead to splat formation and intra-splat and inter-splat-pores as well as cracks in the coating. Due to the demanding conditions including recurrent startups and shutdowns of a gas turbine, the cubic phase transformation is favored by a reduction in the yttria content of the t´ phase. It also causes variations in the lattice parameters of each phase, which indirectly accelerate the failure of the components by thermo-mechanical fatigue [49,50].

In order to account for the effect of prolonged exposure to high temperature, Fig. 15 presents three XRD patterns taken at room temperature for samples treated at 1100 °C with holding times of 600, 1000, and 1700 h. The corresponding phase quantification, obtained from Rietveld refinement, is presented in Table 3. The standard deviation of the values presented in Table 3 was around 0.38 wt% with a maximum of 0.43 wt% for the phase content, and between 0.21 mol% and 0.25 mol% for the $YO_{1.5}$ content in the tetragonal phase. When these results are compared to those obtained at high temperatures and holding time of 10 min in the X-Ray Diffractometer, it can be easily seen that the amount of phases transformed increases with longer holding times.

The tetragonal phase starts transforming into cubic and later into monoclinic phases. In as-sprayed condition, the TC was practically all-tetragonal. At high temperatures and longer exposure times, the yttrium diffusion from the tetragonal phase starts to stabilize the cubic phase.

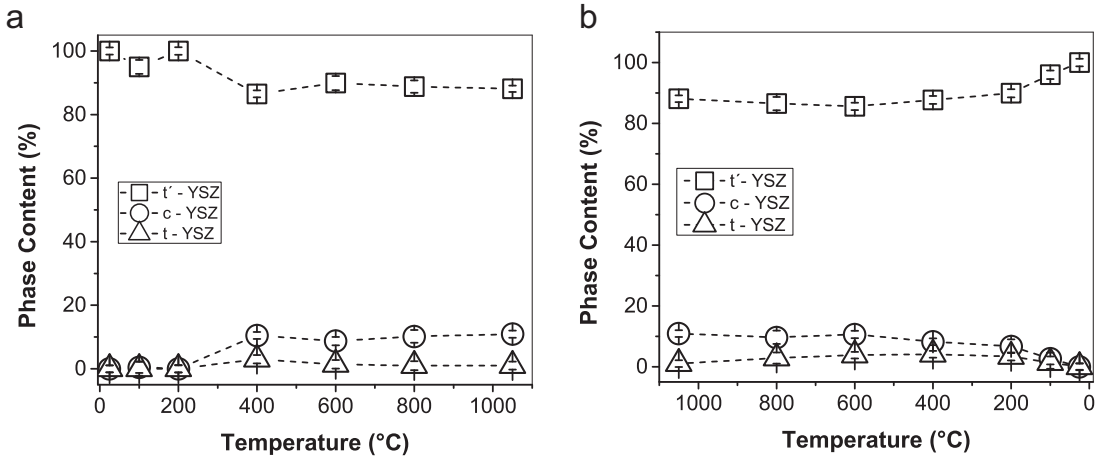

Fig. 14. Phase content in the TC measured by high-temperature XRD: a) Heating, b) Cooling.

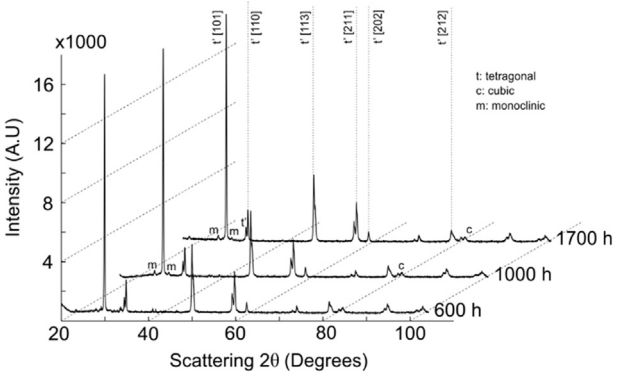

Fig. 15. X-Ray Diffractograms taken at room temperature for thermally treated samples at 1100 °C during 600, 1000, and 1700 h.

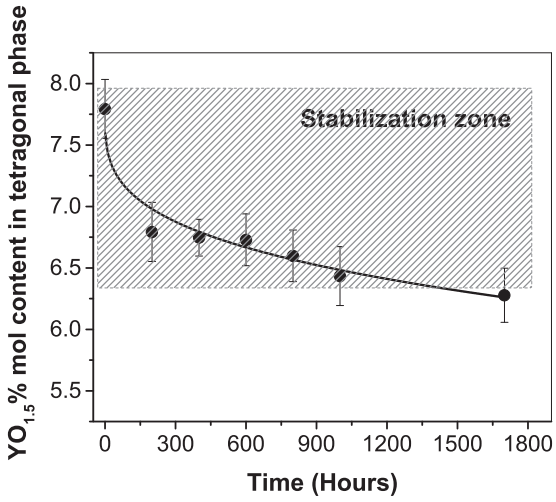

Fig. 16. Variation of yttria content in the tetragonal phase of heat treated samples at 1100 °C.

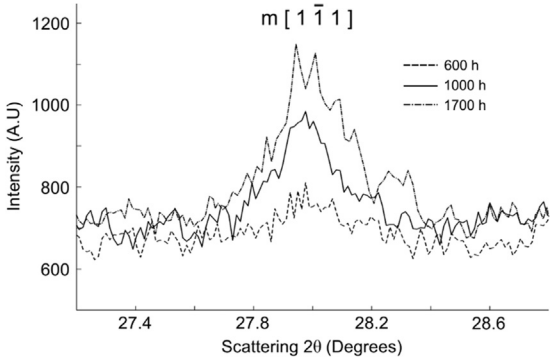

Fig. 17. Close-up of the X-Ray Diffraction pattern in the region close to the monoclinic peak [1$\bar{1}$1] for thermally treated samples at 1100 °C during 600, 1000, and 1700 h.

After 600 h, the $YO_{1.5}$ content in the tetragonal phase reduces from 7.79 mol% to 6.73 mol% (see Fig. 16), leading to a cubic phase stabilization whose content increased from 0.1 wt% to 13.6 wt% (see Table 3). At this time, the $YO_{1.5}$ content in the tetragonal phase had reached a destabilization value where a fraction of this phase transform into 0.4 wt% monoclinic phase after cooling. Tetragonal to monoclinic transformation is not desirable because volumetric changes associated to this transformation can cause TC cracking and reduce its expected lifetime. The monoclinic phase continues growing (see Fig. 17) at the expense of the Y-depleted tetragonal phase reaching about 18.0 wt% after 1000 h at 1100 °C, as can be seen in Table 3. By this time, the tetragonal phase has decreased to 66.3 wt%, while the cubic phase has increased to 15.7 wt%. Finally, after holding times of 1700 h at 1100 °C, the continued decrease of the $YO_{1.5}$ content in the tetragonal phase, as shown in Fig. 16, only favors the stabilization of the monoclinic phase reaching an amount of about 23.4 wt% while the cubic content remains basically invariable from 1000 to 1700 h.

4. Conclusions

Thermal analysis of as-sprayed free-standing YSZ TC samples allowed correlating variations in thermal properties with the stability of the phases in the microstructure. The detailed characterization of the TC included identification and quantification of globular, intra-lamellar, trans-lamellar, and inter-lamellar pores, as well as cracks.

XRD and thermal analyses allowed observing that a high degree of microstructural instability in YSZ TCs is due to phase transformations that occur during heating in the range between 400 and 800 °C; during cooling, there is a partial stabilization of the tetragonal phase in the range from 100 °C to room temperature. With longer exposition times to high temperature, however, the degree of destabilization of tetragonal phase increases due to diffusional processes involving yttrium migration within the microstructure, to te point that after 1700 h at 1100 °C around 15% of cubic phase and 23% of monoclinic phase are formed.

A reduction in the total TC porosity is observed with exposure time during heat treatments at 1100 °C. An initial reduction in the inter-lamellar, intra-lamellar pores and cracks is observed during the first 600 h of heat treatment, mainly due to sintering effects. Then, a slight increase of porosity with exposure time occurs due to the stresses caused by volumetric changes associated to phase transformations. With the increase in exposure time the yttrium diffuses from the metastable tetragonal phase favoring the cubic transformation at high temperature while a fraction of the yttrium depleted tetragonal phase transforms into monoclinic phase after cooling.

The variation of Cp with temperature followed the pattern for the samples according to the literature.

Acknowledgments

The results presented here were possible thanks to the financial support given by *Empresas Públicas de Medellín*, EPM (202010012407). The authors are also grateful to the R&D Department of Argos S.A. for allowing the use of the equipment for thermal analysis.

References

[1] D.R. Clarke, M. Oechsner, N.P. Padture, Thermal-barrier coatings for more efficient gas-turbine engines, MRS Bull. 37 (10) (2012) 891–898.
[2] A. Evans, D. Mumm, J. Hutchinson, Mechanisms controlling the durability of thermal barrier coatings, Prog. Mater. 46 (2001) 505–553.
[3] M.P. Boyce, Gas Turbine Engineering Handbook, Elsevier, Houston, TX, USA, 2012.
[4] Y. Tan, J.P. Longtin, S. Sampath, H. Wang, Effect of the starting microstructure on the thermal properties of as-sprayed and thermally exposed plasma-sprayed YSZ coatings, J. Am. Ceram. Soc. 92 (3) (2009) 710–716.
[5] J. Wu, H. Guo, L. Zhou, L. Wang, S. Gong, Microstructure and thermal properties of plasma sprayed thermal barrier coatings from nanostructured YSZ, J. Therm. Spray Technol. 19 (6) (2010) 1186–1194.
[6] J. Leitner, P. Voňka, D. Sedmidubský, P. Svoboda, Application of Neumann–Kopp rule for the estimation of heat capacity of mixed oxides, Thermochim. Acta 497 (1–2) (2010) 7–13.
[7] X. Song, M. Xie, F. Zhou, G. Jia, X. Hao, S. An, High-temperature thermal properties of yttria fully stabilized zirconia ceramics, J. Rare Earths 29 (2) (2011) 155–159.
[8] Y. Wang, W. Wu, X. Zheng, Y. Zeng, M. Ding, C. Zhang, Relationship between the microstructure and thermal conductivity of plasma-sprayed ZrO_2 coatings, J. Therm. Spray Technol. 20 (6) (2011) 1177–1182.
[9] A. Jadhav, N. Padture, E. Jordan, M. Gell, P. Miranzo, E. Fullerjr, Low-thermal-conductivity plasma-sprayed thermal barrier coatings with engineered microstructures, Acta Mater. 54 (12) (2006) 3343–3349.
[10] R. Taylor, Thermal conductivity determinations of thermal barrier coatings, Mater. Sci. Eng. A 245 (2) (1998) 160–167.
[11] V. Oliker, A. Pritulyak, Effect of the porous structure of thermal barrier coatings on

their heat conductivity, Powder Metall. Met. Ceram. 47 (11) (2008) 717–722.
[12] M.R. Winter, D.R. Clarke, Thermal conductivity of yttria-stabilized zirconia–hafnia solid solutions, Acta Mater. 54 (19) (2006) 5051–5059.
[13] C. Friedrich, R. Gadow, T. Schirmer, Lanthanum hexaaluminate—a new material for atmospheric plasma spraying of advanced thermal barrier coatings, J. Therm. Spray Technol. 10 (4) (2001) 592–598.
[14] I.O. Golosnoy, a. Cipitria, T.W. Clyne, Heat transfer through plasma-sprayed thermal barrier coatings in gas turbines: a review of recent work, J. Therm. Spray Technol. 18 (5–6) (2009) 809–821.
[15] S. Raghavan, H. Wang, R.B. Dinwiddie, W.D. Porter, M.J. Mayo, The effect of grain size, porosity and yttria content on the thermal conductivity of nanocrystalline zirconia, Scr. Mater. 39 (8) (1998) 1119–1125.
[16] J. Zhang, V. Desai, Determining thermal conductivity of plasma sprayed TBC by electrochemical impedance spectroscopy, Surf. Coat. Technol. 190 (1) (2005) 90–97.
[17] B. Siebert, C. Funke, R. Vaβen, D. Stöver, Changes in porosity and Young's modulus due to sintering of plasma sprayed thermal barrier coatings, J. Mater. Process. Technol. 92 (1999) 217–223.
[18] R.A. Miller, J.L. Smialek, R.G. Garlick, Phase stability in plasma-sprayed, partially stabilized zirconia-yttria, Adv. Ceram. 3 (1981) 241–253.
[19] J. Ilavsky, J. Wallace, J.K. Stalick, Thermal spray yttria-stabilized zirconia phase changes during annealing, J. Therm. Spray Technol. 10 (3) (2001) 497–501.
[20] G. Witz, V. Shklover, W. Steurer, S. Bachegowda, H.-P. Bossmann, Phase evolution in yttria-stabilized zirconia thermal barrier coatings studied by Rietveld refinement of X-ray powder diffraction patterns, J. Am. Ceram. Soc. 90 (9) (2007) 2935–2940.
[21] J.R. Brandon, R. Taylor, Phase stability of zirconia-based thermal barrier coatings Part I. Zirconia-yttria alloys, Surf. Coat. Technol. 46 (1) (1991) 75–90.
[22] U. Schulz, Phase transformation in EB-PVD yttria partially stabilized zirconia thermal barrier coatings during annealing, J. Am. Ceram. Soc. 83 (4) (2000) 904–910.
[23] A. Azzopardi, R. Mévrel, B. Saint-Ramond, E. Olson, K. Stiller, Influence of aging on structure and thermal conductivity of Y-PSZ and Y-FSZ EB-PVD coatings, Surf. Coat. Technol. 177 (2004) 131–139.
[24] J. Katamura, T. Sakuma, Computer simulation of the microstructural evolution during the diffusionless cubic-to-tetragonal transition in the system ZrO–Y_2O_3, Acta Mater. 46 (5) (1998) 1569–1575.
[25] ASTM International, ASTM E112 Standard Test Methods for Determining Average Grain Size, 13 (1996), pp. 1–28.
[26] P. Thompson, D.E. Cox, J.B. Hastings, Rietveld refinement of Debye-Scherrer synchrotron X-ray data from Al_2O_3, J. Appl. Crystallogr. 20 (2) (1987) 79–83.
[27] L.B. McCusker, R.B. Von Dreele, D.E. Cox, D. Louer, P. Scardi, Rietveld refinement guidelines, J. Appl. Crystallogr. 32 (1) (1999) 36–50.
[28] W. Beele, G. Marijnissen, A. Van Lieshout, The evolution of thermal barrier coatings—status and upcoming solutions for today's key issues, Surf. Coat. Technol. 120 (1999) 61–67.
[29] A. Cipitria, I.O. Golosnoy, T.W. Clyne, A sintering model for plasma-sprayed zirconia thermal barrier coatings. Part II: coatings bonded to a rigid substrate, Acta Mater. 57 (4) (2009) 993–1003.
[30] J.A. Thompson, W. Ji, T. Klocker, T.W. Clyne, Sintering of the top coat in thermal spray TBC systems under service conditions, Superalloys 2000 (2000) 685–692.
[31] J. Sauvola, M. Pietikäinen, Adaptive document image binarization, Pattern Recognit. 33 (2000) 225–236.
[32] A. Davis, A. Evans, A protocol for validating models of the cyclic undulation of thermally grown oxides, Acta Mater. 53 (2005) 1895–1905.
[33] A. Rabiei, A.G. Evans, Failure mechanisms associated with the thermally grown oxide in plasma-sprayed thermal barrier coatings, Acta Mater. 48 (2000) 3963.
[34] J.D. Osorio, J.P. Hernández, A. Toro, Microstructure characterization of thermal barrier coating systems after controlled exposure to a high temperature, Ceram. Int. 40 (3) (2014) 4663–4671.
[35] L.C. De Jonghe, M.N. Rahaman, Sintering of ceramics, in: Shigeyuki Somiya, Fritz Aldinger, Richard M. Spriggs, Kenji Uchino, Kunihito Koumoto, Masayuki Kaneno (Eds.), Handbook of Advanced Ceramics: Materials, Applications, Processing and Properties, 1–2 2003, pp. 187–264.
[36] A. Ganvir, N. Markocsan, S. Joshi, Influence of isothermal heat treatment on porosity and crystallite size in axial suspension plasma sprayed thermal barrier coatings for gas turbine applications, Coatings 7 (4) (2017) 1–14.
[37] J.A. Thompson, W. Ji, T. Klocker, T.W. Clyne, P. Street, C. Cb, Sintering of the top coat in thermal spray TBC systems under service conditions, Superalloys (2000) 685–692.
[38] A. Cipitria, I.O. Golosnoy, T.W. Clyne, A sintering model for plasma-sprayed zirconia TBCs. Part I: free-standing coatings, Acta Mater. 57 (4) (2009) 980–992.
[39] G.C.C. Costa, S.V. Ushakov, R.H.R. Castro, A. Navrotsky, R. Muccillo, Calorimetric measurement of surface and interface enthalpies of yttria-stabilized zirconia (YSZ), Chem. Mater. 22 (9) (2010) 2937–2945.
[40] C. Degueldre, P. Tissot, H. Lartigue, M. Pouchon, Specific heat capacity and Debye temperature of zirconia and its solid solution, Thermochim. Acta 403 (2) (2003) 267–273.
[41] Z. Lu, S. Myoung, H. Kim, M. Kim, J. Lee, Y. Jung, J. Jang, U. Paik, Microstructure evolution and interface stability of thermal barrier coatings with vertical type cracks in cyclic thermal exposure, J. Therm. Spray Technol. 22 (5) (2013) 671–679.
[42] T. Tojo, H. Kawaji, T. Atake, Molecular dynamics study on lattice vibration and heat capacity of yttria-stabilized zirconia, Solid State Ion. 118 (3–4) (1999) 349–353.
[43] T. Tojo, T. Atake, T. Mori, H. Yamamura, Heat capacity and thermodynamic functions of zirconia and yttria-stabilized zirconia, J. Chem. Thermodyn. 31 (7) (1999) 831–845.
[44] T. Tojo, T. Atake, T. Mori, H. Yamamura, Excess heat capacity in yttria stabilized zirconia, J. Therm. Anal. 57 (2) (1999) 447–458.
[45] R. McPherson, A review of microstructure and properties of plasma sprayed ceramic coatings, Surf. Coat. Technol. 39 (1989) 173–181.
[46] E. Tzimas, H. Müllejans, S. Peteves, J. Bressers, W. Stamm, Failure of thermal barrier coating systems under cyclic thermomechanical loading, Acta Mater. 48 (2000) 4699–4707.
[47] L. Xie, E.H. Jordan, N.P. Padture, M. Gell, Phase and microstructural stability of solution precursor plasma sprayed thermal barrier coatings, Mater. Sci. Eng. A 381 (1) (2004) 189–195.
[48] J.R. Van valzah, H.E. Eaton, Cooling rate effects on the tetragonal to monoclinic phase transformation in aged plasma-sprayed yttria partially stabilized zirconia,", Surf. Coat. Technol. 46 (3) (1991) 289–300.
[49] J.C. Hamilton, A.S. Nagelberg, In situ Raman spectroscopic study of yttria stabilized zirconia attack by molten sodium vanadate, J. Am. Ceram. Soc. 67 (10) (1984) 686–690.
[50] I.O. Golosnoy, S.A. Tsipas, T.W. Clyne, An analytical model for simulation of heat flow in plasma-sprayed thermal barrier coatings, J. Therm. Spray Technol. 14 (2) (2005) 205–214.